ELSEVIER

Volume 181, Number 8, August 2008

JOURNAL OF SOLID STATE CHEMISTRY

www.elsevier.com/locate/jssc

CONTENTS

Abstracted/indexed in BioEngineering Abstracts, Chemical Abstracts, Coal Abstracts, Current Contents/Physics, Chemical, & Earth Sciences, Engineering Index, Research Alert, SCISEARCH, Science Abstracts, and Science Citation Index. Also covered in the abstract and citation database SCOPUS®. Full text available on ScienceDirect®.

Regular Articles

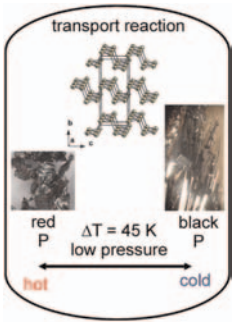

A low-pressure transport reaction route representing the first effective and scalable access to black phosphorus.

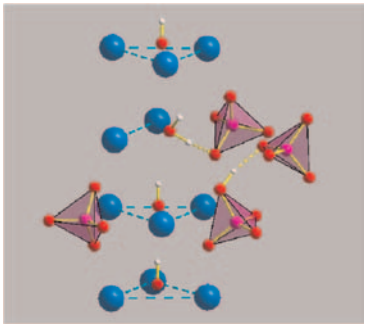

Preferred constellation of a Ca vacancy in hydroxyapatite, accompanied by a H_2O defect and a HPO_4^{2-} defect adjacent to the deficient Ca site. The preferential defect arrangement reflects a compromise of local charge compensation, different proton affinities of the anions and hydrogen bonding.

Regular Articles—Continued

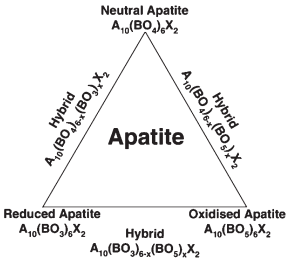

Apatite framework taxonomy succinctly rationalises the crystallographic modifications of this structural family as a function of chemical composition. Neutron diffraction identified that the excess oxygen in $La_9SrGe_6O_{26.5}$ is tenanted in the framework as $[La_9Sr][(GeO_4)_{5.5}(GeO_5)_{0.5}]O_2$. The implication of this approach is that in addition to the three known apatite genera—$A_{10}(BO_3)_6X_2$, $A_{10}(BO_4)_6X_2$, $A_{10}(BO_5)_6X_2$—hybrid electrolytes of the types $A_{10}(BO_3/BO_4/BO_5)_6X_2$ can be designed.

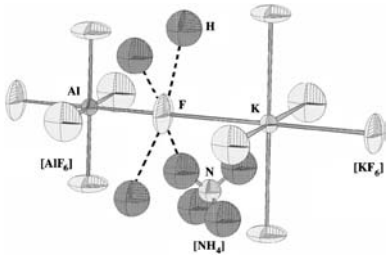

Abnormal anisotropic thermal parameters of fluorine atoms have been observed in the compound $[(NH_4)_{1-x}K_x]_2KAlF_6$ ($x \approx 0.17$), and interpreted to arise from four strong hydrogen bonds (F…H–N) that are distributed in a square form around each fluorine atom. The endmembers' phase transitions at low temperature are believed to be caused by them.

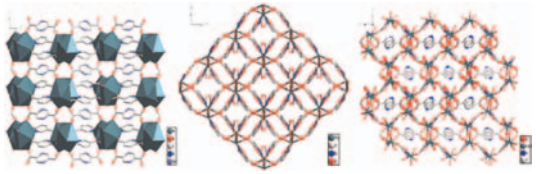

Four new lanthanide coordination polymers have been hydrothermally synthesized by the reaction of 2,5-pyridinedicarboxylic acid with the corresponding lanthanide nitrates, and they show three types of 3D open-framework architecture. Complexes **2** and **5** show strong characteristic green (or red) luminescence and long lifetimes.

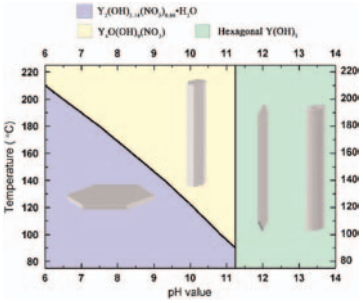

Y_2O_3 particles in the shape of sheet, rod, needle and tube with controlled size were synthesized from three precursors, $Y_2(OH)_{5.14}(NO_3)_{0.86}\cdot H_2O$, $Y_4O(OH)_9(NO_3)$ and hexagonal $Y(OH)_3$, obtained by hydrothermal reactions with controlled pH value and reaction temperature.

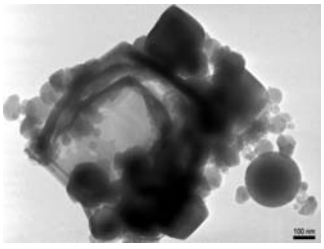

Transmission electron micrograph of $CaAl_2O_4$-microsilica mixture hydrated at 90 °C for 31 days showing a cubic $Ca_3Al_{2.0\pm0.2}(SiO_4)_{0.9\pm0.2}(OH)_{1.8}$ crystal surrounded by unreacted amorphous silica spheres.

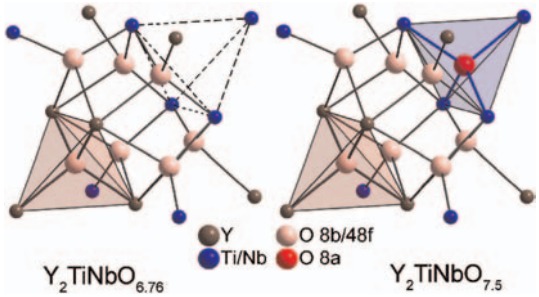

Synthesis of pyrochlore solid solutions $(Y,Lu)_2Ti_{2-x}(Nb,Ta)_xO_{7\pm y}$ under high vacuum at 1600 °C results in oxygen deficient, paramagnetic compounds with reduced *B*-site cations. Studies indicate Ti^{3+} as the source of the localized moments, with no evidence for localized Nb^{4+} moments. Annealing under O_2 results in fully oxidized, oxygen excess pyrochlores as white powders. Powder neutron diffraction studies show the excess oxygen on the normally vacant 8*a* site.

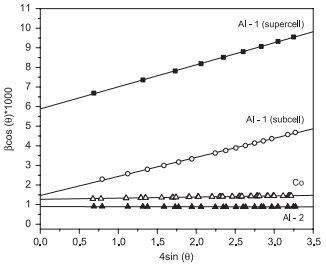

Williamson–Hall plot of the diffraction peaks in Sr2AlSbO6, samples 1 and 2, and in Sr_2CoSbO_6. β denotes the integral breadth corrected for instrumental effects, θ is the diffraction angle. It can be seen that in the case of sample 1, β of the superstructure reflections (solid squares) are clearly larger than those of the rest of the peaks. It was found that depending on the preparation conditions, the Al^{3+} and Sb^{5+} cations can be either entirely or partially ordered. In the case of the partially ordered Sr_2AlSbO_6 sample, the extension of cation ordering was estimated from the *h k l*-dependent broadening of the diffraction peaks and the results were interpreted as evidence of the formation of anti-phase domains in the material. In the case of Sr_2CoSbO_6, despite the high synthesis temperature (1770 K), the degree of ordering is relatively low. This can be explained by the small difference between the radii of the B-site cations. Another interesting fact is that the sample-related broadening of the diffraction peaks of Sr_2CoSbO_6 does not show any significant *h k l*-dependence. This suggests that no extended anti-phase boundaries are formed within the crystallites and the observed low degree of ordering is caused by randomly distributed anti-site defects. In the case of trigonal perovskites the effect of the cation ordering on the peak widths cannot be visualized easily as in the case of cubic perovskites due to the overlapping of the order-related reflections with sub-cell reflections.

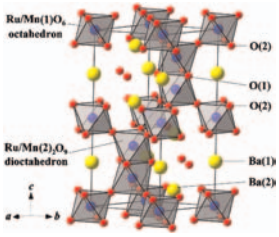

The 6H $BaRu_{1-x}Mn_xO_3$ was synthesized using high-pressure sintering. The substitution of Mn for Ru cations gives rise to the short-range magnetic ordering, with the maximal Curie temperature T_c 175.2 K at $x = 0.10$. The compounds are of spin-class magnetism at lower temperature at $x \geqslant 0.05$. Mn doping results in the transition from the primal metal to semiconductor at $x = 0.30$.

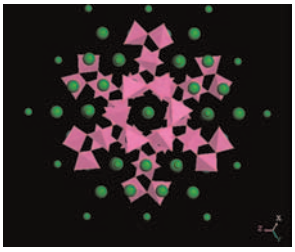

Calcination of a layered double hydroxide precursor produces $Ca_3Al_2O_6$:Eu^{3+}, which is very easy to be pulverized. It is proposed that Eu^{3+} takes the place of one Ca^{2+} (green spheres in the picture, pink pyramids are $[AlO_4]$ tetrahedrons) in the cell of $Ca_3Al_2O_6$. The Ca^{2+} could be any one of the bigger green spheres without inversion symmetry, and emits red light under a UV radiation of $\lambda = 250$ nm.

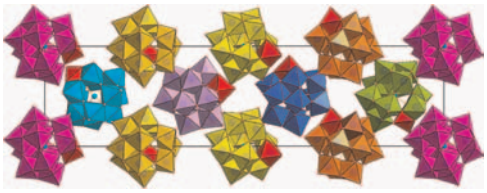

The structure of *ammonium metatungstate* powders are highly dependent on hydration and POM molecule rotation, with cation and hydrogen bonding forces directing a mixture of structures that have been studied with bulk and single-crystal methods. The illustration shows *Monte Carlo* simulated anion structural disorder for the fully dehydrated form of the title compound.

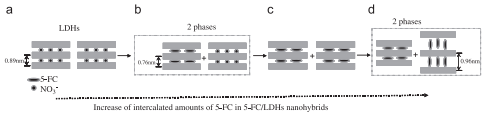

The 5-fluorocytosine (5-FC) has been intercalated into layered double hydroxide using coprecipitation method. The morphology of 5-FC molecules in obtained nanohybrids was dependent on the intercalated amount of 5-FC. The in vitro drug release from the nanohybrids was remarkably lower than that from the corresponding physical mixture, which shows these drug-inorganic nanohybrids can be used as a potential drug delivery system.

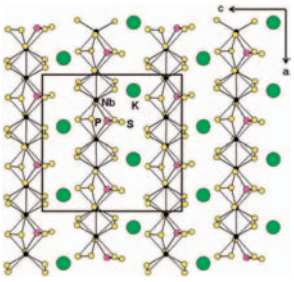

We developed new synthetic routes to obtain 1-D quaternary thiophosphate compounds and a molecular complex containing a Nb_2S_4 core from a 2-D ternary thiophosphate, $Nb_4P_2S_{21}$. When $Nb_4P_2S_{21}$ was reacted with alkali metal halides or TlCl, the –S–S–S– bridges in 2-D Nb_2PS_{10}-S-$S_{10}PNb_2$ were excised to form a 1-D chain, and cations were inserted between the chains.

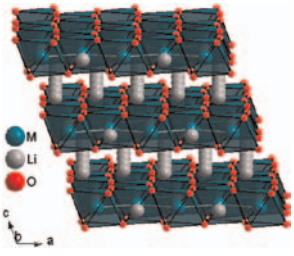

The Li_2IrO_3 and Li_2PtO_3 were synthesized. Refinements are presented along with thermal and electrical properties, which are compared and contrasted with Li_2RuO_3 when appropriate.

Continued

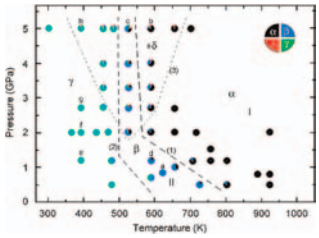

Constructing the pressure–temperature phase diagram for $LiAlO_2$.

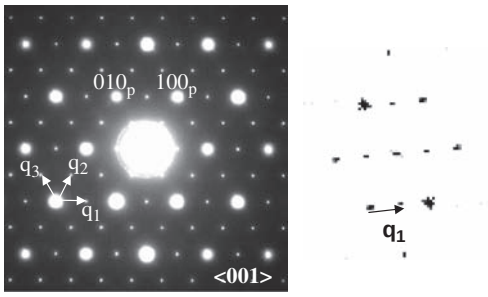

The electron diffraction pattern of $BaAl_2O_4$ (left) is compatible with the 3-**q** superstructure corresponding to the conventional $P6_3$, $\mathbf{a} = 2\mathbf{a}_p$ structure (p refers to the tridymite-related parent $P6_322$ structure). Fast Fourier transforms (right) of small domains of lattice images, however, show that the local structure in fact is single **q**, and that true symmetry is monoclinic or orthorhombic.

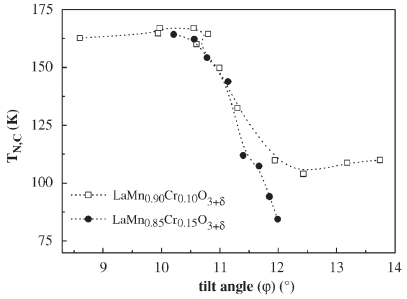

The variation of the critical transition temperature $T_{N,C}$ as a function of the tilt angle "φ" for La $Mn_{0.9}Cr_{0.1}O_{3+\delta}$ and $LaMn_{0.9}Cr_{0.1}O_{3+\delta}$ compounds with $3.00 \leqslant 3+ \cong \leqslant 3.07$ is shown.

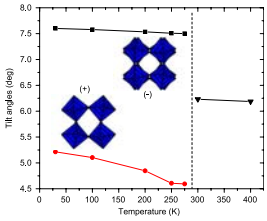

The structure, magnetism, transport and thermal expansion of the perovskite oxide $LaNi_{0.5}Fe_{0.5}O_3$ were studied over a wide range of temperatures. Its structure transforms from orthorhombic at low temperatures to rhombohedral above room temperature. The resistivity and dilatometric data show that this material is compatible with frequently used electrolytes in solid oxide fuel cells.

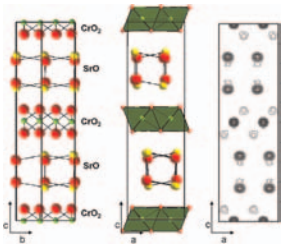

A strontium chromium oxide, $[Sr_2O_2][CrO_2]_{1.85}$, with an orthorhombic misfit layer structure has been synthesised under high pressure. Mainly modulations on the Sr position, ADPs and coordination save the subsystems lattice mismatch.

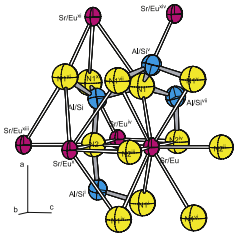

The complete substitution of Ca^{2+} with Sr^{2+} in $CaAlSiN_3$:Eu^{2+} red-emitting phosphor was performed by synthesis at high N_2 gas pressure, analyzed the crystal structure by single-crystal X-ray diffraction, and characterized the photoluminescent properties. The substitution resulted in 4% cell volume increase and 40 nm blue shift of the emission peak, maintaining superior temperature characteristics and oxidative stability.

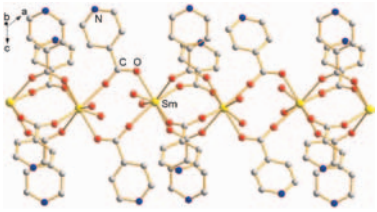

A novel bimetallic 4*f*–3*d* metal–isonicotinic acid inorganic–organic hybrid complex was synthesized. It is characteristic of a one-dimensional polycationic chain-like structure. Photoluminescent investigation reveals that the title complex displays interesting emissions in a wide region. Optical absorption spectra of **1** reveal the presence of a wide optical bandgap.

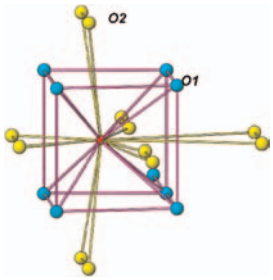

Local surrounding of M ions in $Zr_{0.33}U_{0.67}O_{2.33}$.

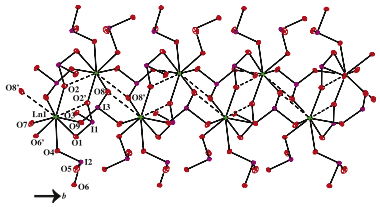

Three *f*-element iodates $Ln(IO_3)_3$ (Ln = Gd, Er, Yb), all containing the $Bi(IO_3)_3$ structure type, were characterized by Raman spectroscopy and magnetic property measurements. The results of the Raman studies indicated that the vibrational profiles are adequately sensitive to distinguish between the structures of the iodates reported here and other lanthanide iodate systems. The magnetic measurements indicate that only in $Gd(IO_3)_3$ did the 3+ lanthanide ion exhibit its full 7.9 μ_B Hund's rule moment; Er^{3+} and Yb^{3+} exhibited ground state moments and gap energy scales of 8.3 μ_B/70 K and 3.8 μ_B/160 K, respectively. $Er(IO_3)_3$ exhibited extremely weak ferromagnetic correlations (+0.4 K), while the magnetic ions in $Gd(IO_3)_3$ and $Yb(IO_3)_3$ were fully non-interacting within the resolution of our measurements (~0.2 K).

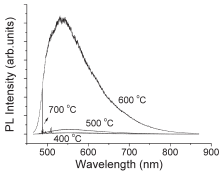

The structural and room temperature photoluminescence of $Ca_xSr_{1-x}WO4$ synthesized by a soft chemical method was studied. The most intense PL emission was obtained for the sample calcined at 600 °C, that is neither highly disordered (400–500 °C), nor completely ordered (700 °C). Corroborating the role of disorder in the PL phenomenon, the most intense PL response was not observed for pure $CaWO_4$ or $SrWO_4$, but for $Ca_{0.6}Sr_{0.4}WO_4$.

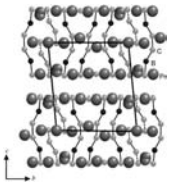

The ternary rare-earth metal boride carbides $RE_{15}B_6C_{20}$ (RE = Pr, Nd) were synthesized by co-melting the elements. They exist above 1270 K. Their structure consists of a three-dimensional framework of rare-earth metal atoms resulting from the stacking of slightly corrugated and distorted square nets, leading to cavities filled with unprecedented B_2C_4 finite chains, disordered C_3 entities and isolated carbon atoms, respectively. Structural and theoretical analyses suggest the ionic formulation $(RE^{3+})_{15}([B_2C_4]^{6-})_3([C_3]^{4-})_2(C^{4-})_2$ 11ē. $Pr_{15}B_6C_{18}$ exhibits antiferromagnetic order at T_N = 7.9 K, followed by a meta-magnetic transition above a critical external field B > 0.03 T. On the other hand, $Nd_{15}B_6C_{18}$ is ferromagnetic below $T_C \approx 40$ K.

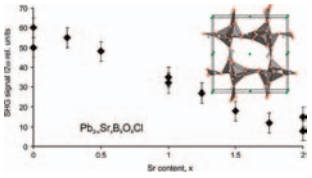

$Sr_2B_5O_9Cl$, $Pb_2B_5O_9Cl$ and the solid solution range $Pb_{2-x}Sr_xB_5O_9Cl$ has been prepared, and studied by powder neutron and X-ray diffraction and SHG measurements.

Continued

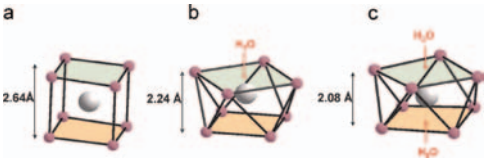

The adaptable environment of U(IV) in U(IV) oxalates: from eight cubic coordination in $U(C_2O_4)_2 \cdot 6H_2O$ (a) completed by water oxygens to nine in $[U(C_2O_4)_2 \cdot H_2O](C_2NH_5)$ (b) and ten coordination in $U(C_2O_4)_2 \cdot 2H_2O$ (c).

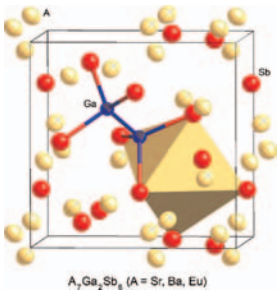

Three new antimonides have been structurally characterized by single-crystal X-ray diffraction. Their structures are best described as derivatives of the body-centered cubic, anti-Th_3P_4 type. Unlike the one-electron-deficient A_4Sb_3 phases (A = Sr, Ba, Eu), the new, $A_7Ga_2Sb_6$ compounds are Zintl phases with closed-shell configurations for both the cations and anions.

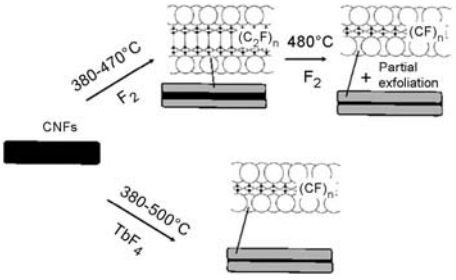

Scheme of the fluorination process using F_2 and TbF_4 as fluorinating agent.

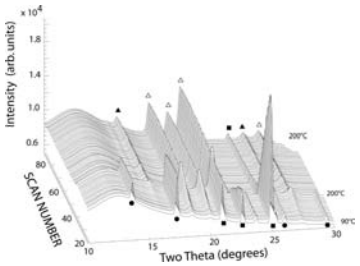

Stack of powder diagrams showing the formation of nanocrystalline ZnSe under hydrothermal conditions.

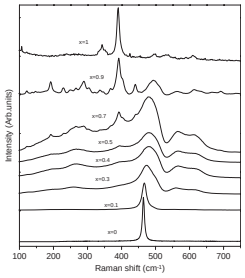

Powder XRD and Raman spectroscopy were used in conjunction to delineate the phases present in CeO_2–Lu_2O_3 and CeO_2–Sc_2O_3 systems. $LuO_{1.5}$ has 30 mol% miscibility, whereas Sc_2O_3 has no discernible solubility in CeO_2. Raman spectroscopy clearly showed the evolution of second phase with change in concentration of the reactants thus supporting XRD data. Back scattered images obtained on representative compositions verify the results.

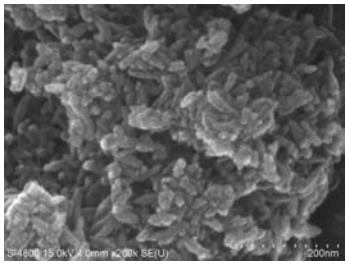

The introduction of surfactant CTAB not only extended the visible light absorption of mesoporous F–N-codoped TiO_2 up to 600 nm but also significantly enhanced the adsorption capacity and visible-light-induced degradation for methyl orange. Mesoporous rod-like F–N-codoped TiO_2 powder photocatalysts were synthesized via a sol–gel route at low temperature of 373 K.

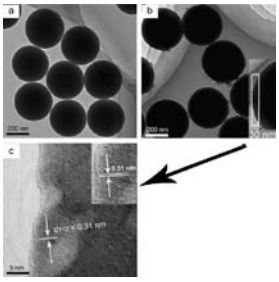

$YNbO_4:Eu^{3+}/Tb^{3+}$ layers were deposited on spherical SiO_2 particles via a sol–gel process, resulting in the formation of core–shell structured $YNbO_4:Eu^{3+}/Tb^{3+}@SiO_2$ phosphors. The luminescence properties of phosphors in the core–shell particles can be tuned by altering the annealing temperature and the coating layers of the phosphors.

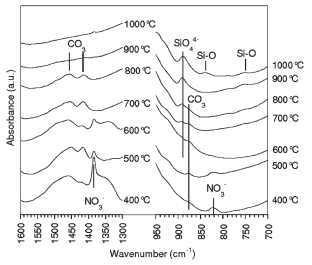

The preparation of pure silicated hydroxyapatite $Ca_{10}(PO_4)_{6-x}(SiO_4)_x(OH)_{2-x}$ powders with controlled silicon content was investigated. The synthesis route included a precipitation in aqueous media. It required an additional high temperature solid-state reaction to fully incorporate the silicon into the apatite crystals.

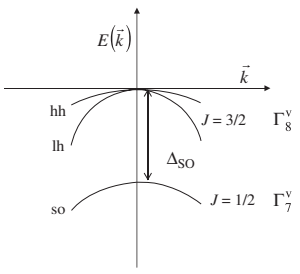

Accounting for *S–D* mixing of hole states, the observed optical transitions in very small sphalerite-type ZnSe and CdSe nanoclusters are attributed to the ground state—($1S_{3/2}$, $1S_e$) and the ground state—($1S_{1/2}$, $1S_e$). The "splittings" do not correspond to SO splitting energy, but are complex functions of it.

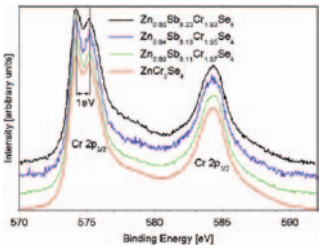

XPS spectrum of Cr2*p* core-levels in the $(Zn_{1-x}Sb_x)[Cr_{2-x/3}]Se_4$ system ($x = 0.11$, 0.16 and 0.20).

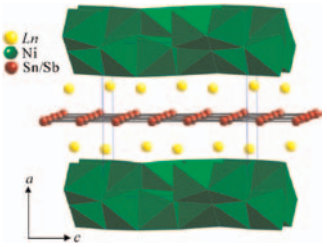

Five new single crystalline analogues of the β-$LnNiSb_3$ family (Ln = Pr, Nd, Sm, Gd, or Tb) have been synthesized and determined to be $LnNi(Sn,Sb)_3$. The structures are compared to the previously reported β-$CeNiSb_3$. Magnetic and transport behavior are reported and discussed.

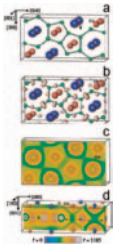

The compounds of rare-earth metals with rhodium and boron $RERhB_4$ (RE = Y, Dy–Lu) crystallize with the orthorhombic structure type $YCrB_4$. Analysis of chemical bonding for $YRhB_4$ and $YbRhB_4$ was performed by electron localizability indicator and by calculation of quantum chemical charges (quantum theory of atoms in molecules). Boron and rhodium form the 3-D polyanion containing planar nets of three-bonded boron atoms interconnected by rhodium along [001]. The interaction of the *RE* species with the rhodium–boron polyanion is predominantly ionic.

Continued

Chemical equilibria involved in the oxygen-releasing step of manganese ferrite water-splitting thermochemical cycle
L. Seralessandri, M. Bellusci, C. Alvani, A. La Barbera, F. Padella and F. Varsano
Page 1992

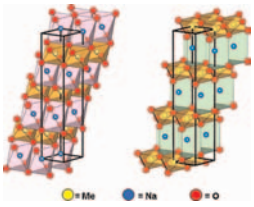

$Na(Mn_{1/3}Fe_{2/3})O_2$ disproportion reaction in the presence of CO_2 was studied. Chemical equilibria among $Na_{1-x}(Mn_{1/3}Fe_{2/3})O_2$, $MnFe_2O_4$ and Na_2CO_3 compounds were evidenced and studied by means of Rietveld analysis performed on XRD patterns. Two different sodium-depleted lamellar structures were identified. The role of sodium carbonate formation/dissociation equilibrium in the oxygen-releasing step of the manganese ferrite thermochemical cycle has been highlighted.

Electron charge distribution of $CaAl_{2-x}Zn_x$: Maximum entropy method combined with Rietveld analysis of high-resolution-synchrotron X-ray powder diffraction data
Karin Söderberg, Yoshiki Kubota, Norihiro Muroyama, Daniel Grüner, Arisa Yoshimura and Osamu Terasaki
Page 1998

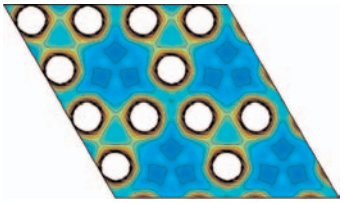

Using short wavelength X-rays from synchrotron radiation (SPring-8), high-resolution powder diffraction patterns of the Laves ($MgCu_2$ and $MgNi_2$ type) and KHg_2-type phases in the $CaAl_{2-x}Zn_x$ system were collected. The charge density distribution in the Laves phases as a function of x was obtained from the diffraction data by Rietveld analysis combined with the maximum entropy method (MEM).

Characterization and reactivity of nanoscale $La(Co,Cu)O_3$ perovskite catalyst precursors for CO hydrogenation
Nguyen Tien-Thao, Houshang Alamdari and Serge Kaliaguine
Page 2006

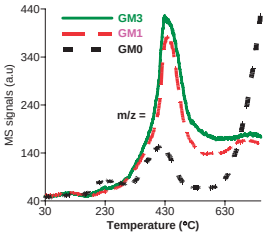

The ground $La(Co,Cu)O_3$ perovskite precursors were reduced as catalysts for CO hydrogenation. The TPSR results show that the presence of a neighboring copper along with remnant sodium ions on the catalyst surface of these solids has remarkably affected the reactivity of cobalt for CO hydrogenation. The addition of copper into the perovskite framework leads to a change in the product distribution of CO hydrogenation and a decrease in reaction temperature. An increased copper content leads to a substantial decline in the rate of methanation and an increase in the formation of higher alcohols.

Fabrication and optical conductivities of strained epitaxial Na_xCoO_2 thin films: $x = 0.5$, 0.7
J.Y. Son, Y.H. Shin and C.S. Park
Page 2020

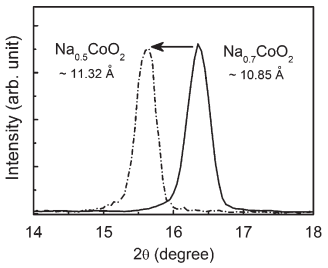

From the spectroscopic ellipsometry analysis, we obtained optical constants as well as optical conductivities for $Na_{0.5}CoO_2$ and $Na_{0.7}CoO_2$ thin films. The energy splitting between e_g and a_{1g} increased as a result of the structural strain of the $Na_{0.7}CoO_2$ thin film.

Structure and physical properties of the new telluride $BaAg_2Te_2$ and its quaternary variants $BaCu_\delta Ag_{2-\delta}Te_2$
Abdeljalil Assoud, Yanjie Cui, Stephanie Thomas, Brodie Sutherland and Holger Kleinke
Page 2024

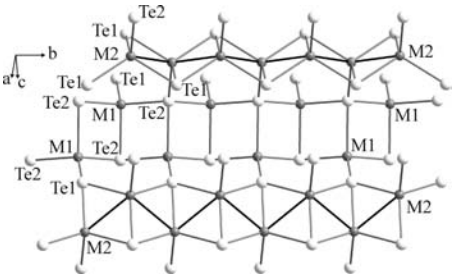

The tellurides $BaCu_\delta Ag_{2-\delta}Te_2$ all crystallize in the α-$BaCu_2S_2$ type. The Ag atoms prefer the $M2$ sites with short M–M bonds (solid lines). The materials are (degenerate) p-type semiconductors. Higher Ag content reflects itself in higher Seebeck coefficient and lower electrical conductivity.

Influence of iron addition on the oxygen-deficient $Sr_{0.85}Bi_{0.15}Co_{1-x}Fe_xO_{3-\delta}$ ($0.0 \leqslant x \leqslant 1.0$) perovskites
Annika K. Eriksson, Fredrik Lindberg, Gunnar Svensson, Peter Svedlindh, Paul F. Henry, Sten-G. Eriksson and Christopher S. Knee
Page 2031

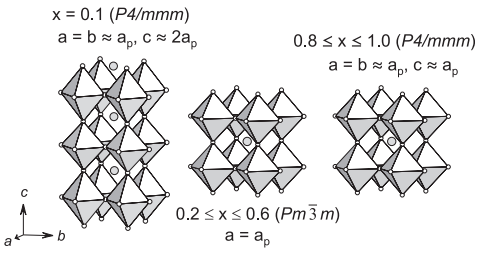

Evolving crystal structures of the as-prepared $Sr_{0.85}Bi_{0.15}Co_{1-x}Fe_xO_{3-\delta}$ perovskites as a function of iron content for the compositional range $0.1 \leqslant x \leqslant 1.0$.

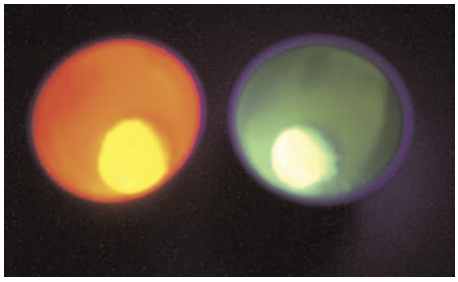

The photoluminescence and radioluminesce emission from rare-earth doped Y_2O_3 nanophosphors are being investigated. Below is a representative image of the photoluminescence from Y_2O_3:Eu^{3+} (left) and Y_2O_3:Tb^{3+} (right) under UV-light excitation.

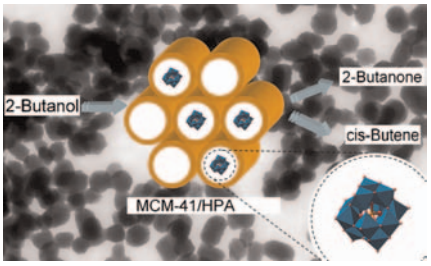

Samples based in MCM-41 nanoparticles loaded with tungstophosphoric and molybdophosphoric acids have been synthesised. The uncalcined solids and that derived upon their calcination in the temperature range 250–550 °C have been characterised and evaluated in the decomposition of 2-butanol monitored by FT-IR spectroscopy.

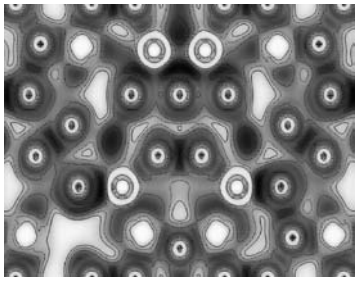

$Mg_2Co_3Sn_{10+x}$ belongs to the fascinating group of compounds combining localized and delocalized chemical bonding of the same element type in their structure. The structural stability up to 9.69 GPa and chemical bonding of this complex metallic alloy (120 atoms per unit cell) is reported.

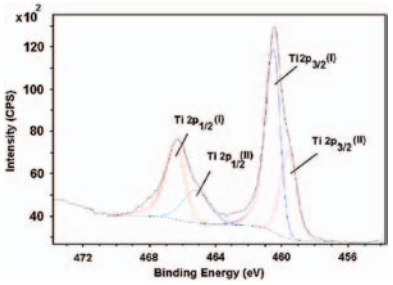

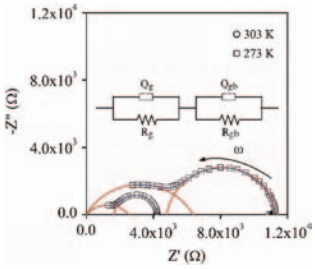

NiO nanocrystals showed distinct low-temperature bulk and grain boundary conductions that are highly dependent on the particle sizes.

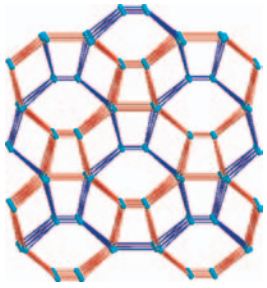

The solvothermal reactions of Cd(II) and Zn(II) salts bearing different anions with 5-amino-1H-1,2,4-triazole-3-carboxylic acid (AmTAZAc) produced four Cd(II) and Zn(II) MOFs with the in situ-generated 3-amino-1,2,4-triazolate ($AmTAZ^-$) ion as ligand, which display different structural topologies and fluorescent properties.

Continued

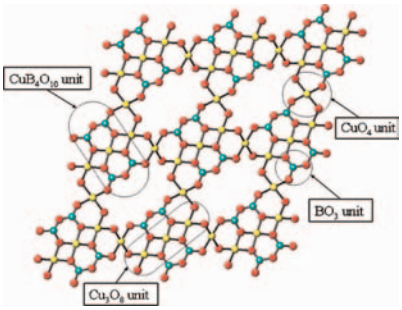

The figure shows a layered structure that is built up from sheets of distorted rectangular CuO_4 and trigonal BO_3 groups. The sheets are connected by infinite chains of edge shared BiO_6 polyhedra that intersect the *bc* plane. These distortions lead to the second-harmonic generation efficiency of $Bi_2Cu_5B_4O_{14}$ about one half times that of KH_2PO_4.

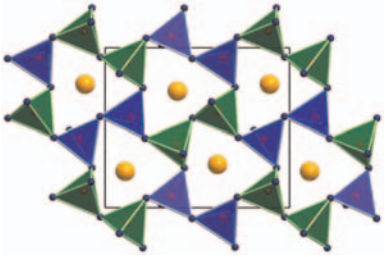

High-pressure/high-temperature synthesis (multianvil technique) led to the new phase α-FeB_2O_4, which is exclusively built up from corner-sharing BO_4-tetrahedra, isotypic to the monoclinic phases *β*-$SrGa_2O_4$, $CaAl_2O_4$-II, and $CaGa_2O_4$.

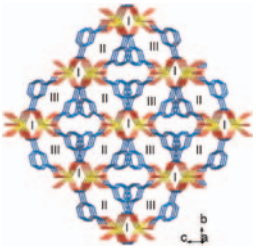

A series of lanthanide coodination polymers, $(Him)_n[Ln(ip)_2(H_2O)]_n$ [Ln = La(**1**), Pr(**2**), Nd(**3**) and Dy(**4**)] and $[Y_2(ip)_3(H_2O)_2]_n \cdot nH_2O$ (**5**), have been reported. The isostructural compounds **1**–**4** possess 3-D structures with three different kinds of channels. Compound **5** displays a 2-D network making of two kinds of quadruple-helical chains.

Rapid Communications

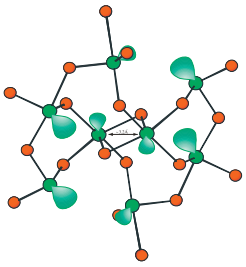

Two unprecedented tellurites, $NH_4ATe_4O_9 \cdot 2H_2O$ (A = Rb or Cs) have been synthesized and characterized. The materials represent rare examples of tellurites that contain TeO_3, TeO_4, and TeO_5 polyhedra in the same compound. All of the polyhedra are in asymmetric polar coordination environments attributable to their stereo-active lone-pair.

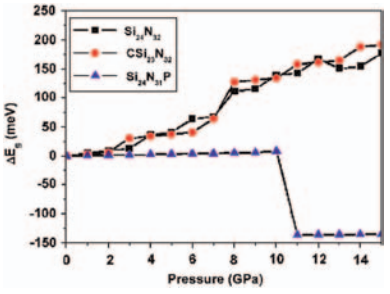

We performed density functional calculations to predict the insulator-to-metal transition by replacing Si by C at the tetrahedral sites of P-doped c-Si_3N_4.

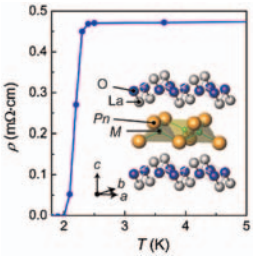

A new layered oxyarsenide, LaNiOAs, which exhibits a superconducting transition at 2.4 K, was synthesized by solid-state reactions. This compound had a tetragonal ZrCuSiAs-type structure similar to recently discovered superconductors, LaFeOP, LaFeOAs, and LaNiOP. Superconductivity was observed for undoped LaNiOAs, which differs from the case of LaFeOAs.

Corrigenda

Corrigendum to "Characterization of $Bi_5Nb_3O_{15}$ by refinement of neutron diffraction pattern, acid treatment and reaction of the acid-treated product with *n*-alkylamines" [J. Solid State Chem. 180 (2007) 2517–2524]

Seiichi Tahara, Akira Shimada, Nobuhiro Kumada and Yoshiyuki Sugahara

Page 2121